Dalton Transactions

ROYAL SOCIETY OF CHEMISTRY

PAPER

View Article Online
View Journal | View Issue

Check for updates

Cite this: *Dalton Trans.*, 2024, **53**, 8191

Magneto-structural correlation in lanthanide luminescent [2.2]paracyclophane-based single-molecule magnets†

Hadrien Flichot,[a] Annika Sickinger,[b] Jules Brom,[c] Bertrand Lefeuvre,[a] Vincent Dorcet,[a] Thierry Guizouarn,[a] Olivier Cador,[a] Boris Le Guennic,[a] Laurent Micouin,[c] Olivier Maury,[b] Erica Benedetti*[c] and Fabrice Pointillart*[a]

The association of lanthanide ions and paracyclophane derivatives has been very scarcely reported in the literature. In this study, elaboration of five coordination lanthanide complexes involving the 1,4(1,4)-dibenzenacyclohexaphane-1^2,4^3-diylbis(diphenylphosphine oxide) ligand (**L**) was achieved with the determination of single-crystal X-ray diffraction structures of four mononuclear complexes of formula [Ln(hfac)$_3$(**L**)] (hfac- = 1,1,1,5,5,5-hexafluoroacetylacetonate) (Ln = Dy(III) (**1-Dy**) and Yb(III) (**2-Yb**)) and [Ln(tta)$_3$(**L**)] (tta$^-$ = 2-tenoyl-trifluoroacetylacetonate) (Ln = Dy(III) (**3-Dy**) and Yb(III) (**4-Yb**)) and one dinuclear complex [Na(Dy$_2$(hfac)$_6$(**L**)$_2$)](BArF) (BArF$^-$ = tetrakis[3,5-bis(trifluoromethyl)phenyl]borate) (**5-Dy**). The compounds were characterized using elemental analysis, IR spectroscopy, DC and AC magnetic measurements and photophysical investigations. L is an efficient organic chromophore for the sensitization of both visible Dy(III) (**1-Dy**) and near-infrared Yb(III) (**2-Yb** and **4-Yb**) luminescence. The combination of excitation and emission spectra allowed the determination of the crystal field spitting of both the $^2F_{7/2}$ ground state and $^2F_{5/2}$ excited state for **2-Yb** and **4-Yb**. Moreover, **3-Dy** and the two Yb(III) derivatives displayed field-induced single-molecule magnet (SMM) behaviour with slow magnetic relaxation occurring through the Raman process only for **2-Yb** and **4-Yb**, whereas a combination of Orbach and Raman processes was identified for **3-Dy**.

Received 23rd February 2024,
Accepted 21st April 2024

DOI: 10.1039/d4dt00536h

rsc.li/dalton

Introduction

Since the end of the 40's and the discovery of the [2.2]paracyclophane (pCp) and its derivatives, their unique structural and electronic properties have made them a centre of interest for chemists.[1] Indeed, these organic molecules are composed of two ethylene arms linking two distorted benzene, which can be decorated with a plethora of chemical groups.[2] [2.2] Paracyclophanes have been successfully exploited in materials science for the development of organic light-emitting diodes (OLEDs) and nonlinear optical materials.[3] The most fascinating property of the pCps is probably their planar chirality.[4] Since their rigid structure precludes any rotational motion of their aromatic rings, all mono-substituted pCps are optically active compounds, and different planar chiral derivatives can be rapidly generated by increasing the number of substituents on the pCp core. The resulting optically active pCp derivatives were exploited to build families of luminescent compounds displaying electronic circular dichroism (ECD) and circularly polarized luminescence (CPL).[5] Moreover, such pCp could be used as ligands for designing coordination complexes or catalysts in asymmetric catalysis and stereoselective synthesis.[6,7]

Focusing on coordination complexes, lanthanide ions are fascinating metal centres due to their magnetic and optical behaviours. On the one hand, their high magnetic moment and strong magnetic anisotropy made it possible to observe a slow magnetic relaxation for a terbium mononuclear complex in 2003,[8] called single-molecule magnet (SMM) behavior,[9] paving the way for potential applications in high-density data storage,[10] quantum computing[11] and spintronics.[12] Then, chemists developed several approaches to enhance the magnetic performances of SMMs, such as the involvement of organic radicals to favour strong magnetic exchange interaction,[13,14]

[a]*Univ Rennes, CNRS, ISCR (Institut des Sciences Chimiques de Rennes) – UMR 6226, 35000 Rennes, France. E-mail: fabrice.pointillart@univ-rennes.fr*
[b]*Univ Lyon, ENS de Lyon, Université Claude Bernard Lyon 1, CNRS UMR 5182, Laboratoire de Chimie, Lyon F-69342, France*
[c]*Université Paris Cité, CNRS, Laboratoire de Chimie et de Biochimie Pharmacologiques et Toxicologiques, F-75006 Paris, France. E-mail: erica.benedetti@u-paris.fr*

†Electronic supplementary information (ESI) available: SCXRD and PXRD data, computational details, DC and AC magnetic data, emission data. CCDC 2297628–2297632. For ESI and crystallographic data in CIF or other electronic format see DOI: https://doi.org/10.1039/d4dt00536h

organometallic chemistry to impose strong uniaxial crystal field and high blocking temperatures[15–18] and metal–metal bond to increase the coercive field.[19] On the other hand, lanthanide ions are well-known for their specific emission line-like spectra and long emission lifetimes,[20–22] finding applications in bioimaging,[23–25] optical telecommunication devices[26–30] and OLEDs.[31,32] For more than a decade, several groups demonstrated that magneto-structural correlation could be established between the magnetic and emissive properties in order to gain deeper insight into the physical behaviour of such systems.[33–39]

The association of lanthanide coordination complexes with chirality paved the way for the observation of new physical properties due to the cross-effect or synergy between two properties. For instance, circularly polarized luminescence and magneto-chiral dichroism (MChD) can be detected with remarkable signal intensities for chiral luminescent magnetic lanthanide complexes.[40–44] In this context, some of us exploited chiral ligands with helicoidal (helicene ligands) and axial (binaphtyl ligands) chirality to design multifunctional materials displaying CPL and/or MChD.[45–48] The use of pCp with planar chirality could be a suitable approach for designing new CPL/MChD active lanthanide systems, allowing us to go further into the origin of these properties by highlighting the role of the type of chirality. However, examples of pCp-based lanthanide compounds are very scarce and have only been studied in their racemic form for their optical properties (emission and singlet oxygen generation).[49,50] To the best of our knowledge, no single-crystal X-ray diffraction structures of these compounds have been reported so far.

In the next lines and as a first step before going to design chiral pCp lanthanide compounds, we proposed to use a racemic [2.2]paracyclophane decorated bisoxophosphine ligand (**L**) to coordinate the building blocks of formula Ln(β-diketonate)$_3$(H$_2$O)$_2$ (Ln = Dy(III) and Yb(III) (β-diketonate = hfac$^-$, 1,1,1,5,5,5-hexafluoroacetylacetonate or tta$^-$, 2-tenoyl-trifluoroacetylacetonate) and extend the rare reported examples of pCp-based lanthanide coordination complexes. Their association led to the formation of four mononuclear complexes [Ln(hfac)$_3$(**L**)] (Ln = Dy(III) (**1-Dy**) and Yb(III) (**2-Yb**)) and [Ln(tta)$_3$(**L**)] (Ln = Dy(III) (**3-Dy**) and Yb(III) (**4-Yb**)) and one dinuclear complex [Na(Dy$_2$(hfac)$_6$(**L**)$_2$)](BArF) (**5-Dy**) in the presence of the bulky tetrakis[3,5-bis(trifluoromethyl)phenyl]borate (BArF$^-$) anion. All molecular structures were elucidated using single-crystal X-ray diffraction, and their magnetic and photophysical properties were investigated. A magneto-structural correlation was performed and rationalized by a computational approach.

Results and discussion

Synthesis of the [2.2]paracyclophane-based bisoxophosphine ligand (L)

The pCp-based ligand **L** was prepared in two steps, starting from commercially available 4,16-dibromo[2.2]paracyclophane (**P1**) *via* an optimization of previously reported procedures. **P1** was first submitted to an isomerization reaction occurring in triglyme at 220 °C under microwave irradiation. This transformation allowed us to isolate the desired racemic 4,12-dibromo[2.2]paracyclophane (**P2**) in 84% yield after purification over silica gel column chromatography. This compound was then submitted to a double bromine-lithium exchange, followed by a reaction with diphenylphosphinyl chloride (2.2 equiv.) to obtain the desired product in 45% isolated yield (Scheme 1). The racemic pCp ligand **L** was used for the preparation of all mononuclear Ln complexes. The latter were easily obtained by an equimolar reaction of **L** with Ln(hfac)$_3$(H$_2$O)$_2$ or Ln(tta)$_3$(H$_2$O)$_2$ (Ln = Dy(III) and Yb(III)).

Crystal structure analysis

[Dy(hfac)$_3$(L)] (1-Dy). **1-Dy** crystallized in the monoclinic space group *P*21/*n* (N°14) (Table S1†). The asymmetric unit is composed of one complex with the formula [Dy(hfac)$_3$(**L**)] (Fig. 1 and Fig. S1†). The Dy(III) centre is surrounded by eight oxygen atoms coming from three hfac$^-$ anions and one bischelating **L**. The average Dy–O$_{P=O}$ bond length (2.249 Å) is shorter than the Dy–O$_{hfac}$ bond length (2.385 Å). The arrangement of the ligands around the lanthanide ion leads to a dodecahe-

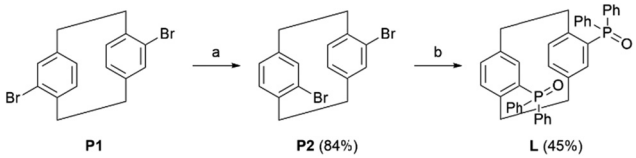

Scheme 1 Synthetic route for **L** with reaction conditions: (a) μW, triglyme, 220 °C, 2 h (three iterations); (b) *t*-BuLi (1M in THF, 4 equiv.), THF, −78 °C to rt, 15 min, then Ph$_2$POCl (2.2 equiv.), rt, 2 h.

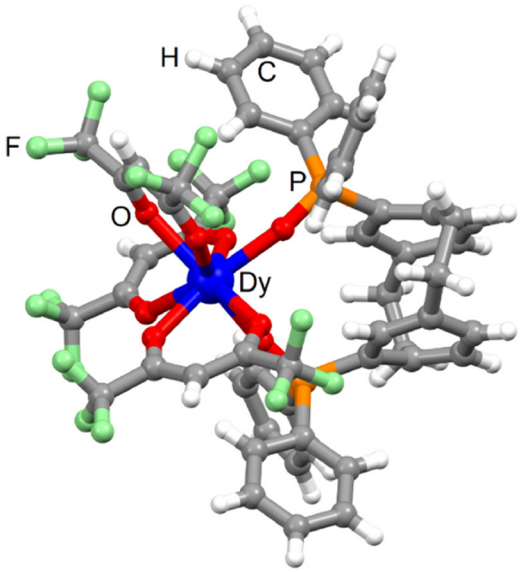

Fig. 1 Molecular structure of **1-Dy**. Colour code: white, H; grey, C; green, F; red, O; orange, P; blue, Dy.

dron (D_{2d} symmetry) as coordination polyhedra. The distortion is visualized by continuous shape measures performed with SHAPE 2.1 (Table S2†).[51] The single crystal of **1-Dy** contains a 1 : 1 mixture of Rp and Sp enantiomers of **L**. The torsion angle between the benzene rings of the paracyclophane moiety is ±24.6°. The crystal packing revealed π-interactions between the phenyl rings of the pCp and diphenyl oxo-phosphine groups (Fig. S2†). The shortest Dy⋯Dy distance was measured at 11.618 Å. All the complexes in the (110) plane (Fig. S2†) involved L ligand with the same chirality while the neighbouring plane contains complexes with ligand **L** of opposite chirality. The phase purity was checked by powder X-ray diffraction comparing the experimental PXRD of **1-Dy** with the simulated PXRD obtained from the single crystal X-ray structure (Fig. S3†).

[Yb(hfac)$_3$(L)] (2-Yb). **2-Yb** crystallized in the tetragonal space group $I4_1/acd$ (N°142) (Fig. S4 and Table S1†). The asymmetric unit is composed of a one-half complex of **2-Yb**. One could notice that **2-Yb** crystallizes in a different space group than **1-Dy**, which might be due to the smaller ionic radius of Yb(III) compared to Dy(III). Nevertheless, the complex formed is very similar to **1-Dy**, with the three ancillary hfac$^-$ ligands being 50/50% disordered in two positions. The average Yb–$O_{P=O}$ and Yb–O_{hfac} bond lengths are equal to 2.188 Å and 2.336 Å, respectively. The torsion angle is ±22.4° and the shortest Yb⋯Yb intermolecular distance is equal to 12.148 Å. The phase purity was checked by powder X-ray diffraction comparing the experimental PXRD of **2-Yb** with the simulated PXRD obtained from the single crystal X-ray structure (Fig. S5†).

[Ln(tta)$_3$(L)] Ln = Dy (3-Dy) and Yb (4-Yb). Both compounds are isomorphous and only the molecular structure of **3-Dy** is described with numerical values for **4-Yb** in square brackets. **3-Dy** crystallized in the monoclinic space group $P2_1/n$ (N°14) (Table S1†). The asymmetric unit is composed of one complex with the formula [Dy(tta)$_3$(**L**)] (Fig. 2 and Fig. S6† for **3-Yb** and Fig. S7† for **4-Yb**).

The Dy(III) centre is surrounded by eight oxygen atoms coming from three tta$^-$ anions and one bischelating **L**. The average Dy–$O_{P=O}$ bond length (2.265 Å) [2.222 Å] is shorter than the Dy–O_{tta} one (2.374 Å) [2.344 Å] and they are close to those found for **1-Dy**. The replacement of hfac$^-$ with tta$^-$ did not change the arrangement of the ligands around the lanthanide ions. The coordination polyhedron keeps the dodecahedron prism (D_{2d} symmetry) with a similar distortion from the ideal symmetry than the one calculated for **1-Dy** [**3-Dy**] and **2-Yb** [**4-Yb**] (Table S2†).[51] The torsion angle was measured at ±23.6° [22.4°]. Intramolecular S⋯S contacts were identified with the S2⋯S3 short contact (3.631 Å) [3.590 Å]. Crystal packing revealed π-interactions between the phenyl rings of the pCp and diphenyl oxo-phosphine groups and additional intermolecular S2⋯S2 short contact (3.601 Å) [3.678 Å] (Fig. S8†). The shortest Dy⋯Dy distance was measured to be 11.163 Å [11.217 Å]. The phase purity was checked using powder X-ray diffraction comparing the experimental PXRD of **3-Dy** with the simulated PXRD obtained from the single crystal X-ray diffraction (Fig. S9†).

[Na(Dy$_2$(hfac)$_6$(L)$_2$)](BArF) (5-Dy). **5-Dy** was obtained as **1-Dy** in the presence of an excess of NaBArF salt. **5-Dy** crystallized in the triclinic space group $P\bar{1}$ (N°2) (Table S1†). The asymmetric unit is composed of two [Dy(hfac)$_3$(**L**)] complexes, one Na(I) cation and one BArF$^-$ anion (Fig. 3 and Fig. S10†).

5-Dy can be seen as two **1-Dy** complexes linked by a sodium cation. The latter is eight coordinated to four fluorine atoms (Na–F = 2.416 Å) and four oxygen atoms (Na–O = 2.435 Å) from the hfac$^-$ ligand. Such an assembly is surprising because some of us showed that the Ln(hfac)$_3$ building block is able to release a β-diketonate in the presence of NaBArF salt.[52] The sodium cation links two complexes involving **L** with opposite chirality. The torsion angles are −23.9° and +15.1° for the pCp,

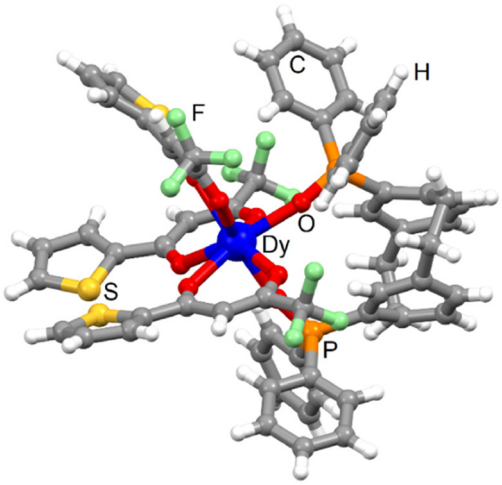

Fig. 2 Molecular structure of **3-Dy**. Code colour: white, H; grey, C; green, F; red, O; orange, P; yellow, S; blue, Dy.

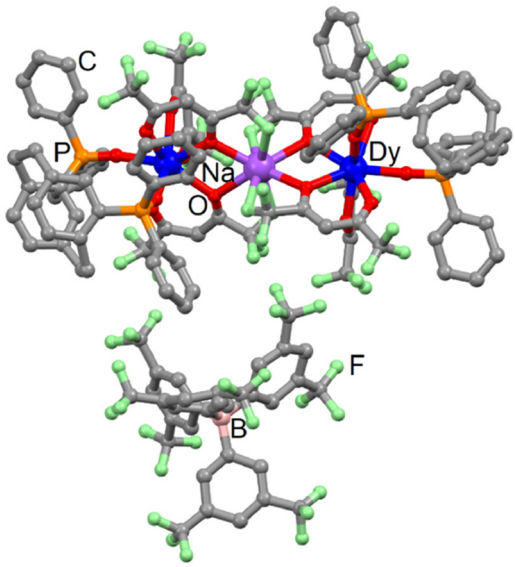

Fig. 3 Molecular structure of **5-Dy**. Code colour: grey, C; green, F; red, O; orange, P; purple, Na; blue, Dy.

respectively, coordinated to the Dy1 and Dy2 centres. The average Dy···Na distance is 3.935 Å while the intramolecular Dy···Dy distance is 7.846 Å. Moreover, the shortest intermolecular Dy···Dy distance is 11.826 Å. The crystal packing highlighted that the $BArF^-$ anion prevents π-interactions between the phenyl rings of paracyclophane and bisphenyl oxophosphine groups (Fig. S11†).

Magnetic investigations

The temperature dependence of $\chi_M T$ for samples **1–5** are represented in Fig. 4. Room temperature values are 13.74 cm^3 K mol^{-1}, 2.37 cm^3 K mol^{-1}, 13.39 cm^3 K mol^{-1}, 2.26 cm^3 K mol^{-1} and 26.56 cm^3 K mol^{-1} for **1–5**, respectively. Such values are in agreement with the expected values of 14.17 cm^3 K mol^{-1} (for one Dy(III) with a $^6H_{15/2}$ ground state (GS) and g_J = 4/3), 2.57 cm^3 K mol^{-1} (for one Yb(III), $^2F_{7/2}$ GS, g_J = 8/7) and 28.34 cm^3 K mol^{-1} for two Dy(III) ions.[53,54] Upon cooling, $\chi_M T$ decreases monotonically down to 10.55 cm^3 K mol^{-1}, 1.00 cm^3 K mol^{-1}, 11.10 cm^3 K mol^{-1}, 0.84 cm^3 K mol^{-1} and 19.12 cm^3 K mol^{-1} for **1–5**, respectively. Such a decrease could be attributed to both thermal depopulation of the m_J states of the Dy(III) and Yb(III) ions and antiferromagnetic interactions between the different magnetic centres. Magnetizations for **1–5** at 2 K are depicted in Fig. S12† with experimental values of 4.86$N\beta$, 1.47$N\beta$, 5.02$N\beta$, 1.46$N\beta$ and 9.89$N\beta$ at 50 kOe, respectively. DC magnetic measurements show that the two Yb(III) derivatives have very similar magnetic behaviour while significant differences are observed for the Dy(III) derivatives. One could thus anticipate very similar dynamic magnetic behaviour for the two Yb(III) derivatives while some differences may appear for the two Dy(III) derivatives.

As shown in Fig. 4 and Fig. S12,† DC magnetic data are well corroborated by the results of *ab initio* calculations (see computational details in Experimental section) on **1-Dy**, **2-Yb**, **3-Dy** and **4-Yb**. As already seen in previous works,[55,56] while a good agreement is obtained at the CASSCF level for the Dy complexes, adding dynamical correlation through perturbative treatment is mandatory for the Yb systems. Computed energy and wavefunction composition for each M_J state of the ground-state multiplet as well as component values of the Lande g factor are given in Tables S9–S12.† In particular, one may notice the highly mixed composition of the ground state wavefunction of **2-Yb** and **4-Yb** that precludes any exciting SMM behaviour. For the Dy derivatives, while **1-Dy** presents a GS with non-negligible $|\pm 13/2\rangle$ contribution and extremely close first excited state, **3-Dy** behaves differently with a well-separated ground state mainly composed of $M_j = |\pm 15/2\rangle$ giving rise to Ising g-tensor ($g_x = g_y = 0$; $g_z = 19.5$), a prerequisite for observing SMM behaviour.

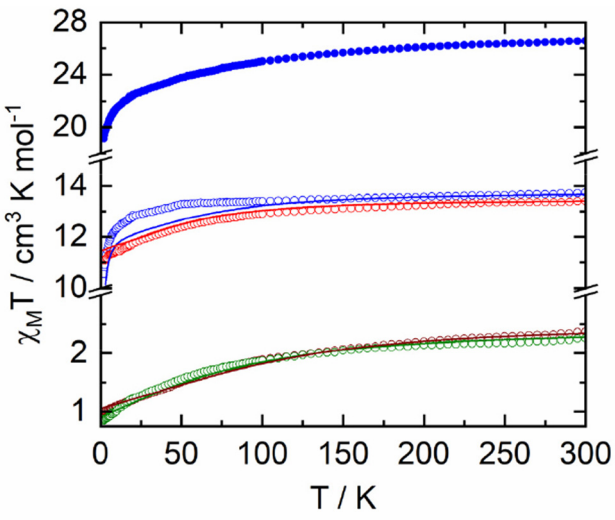

Fig. 4 Temperature dependence of $\chi_M T$ for **1-Dy** (open blue circles), **2-Yb** (open wine circles), **3-Dy** (open red circles), **4-Yb** (open green circles) and **5-Dy** (full blue circles). Full lines correspond to calculated data.

The in-phase (χ'_M) and out-of-phase (χ''_M) components of the AC magnetic susceptibility for compounds **1–5Ln** were measured using immobilized selected and crunched single crystals. For both compounds **1-Dy** and **5-Dy**, no out-of-phase signal was detected in zero and applied magnetic field in the 1–10 000 Hz frequency range and at 2 K. The three other compounds **2–4Ln** did not display any χ''_M contribution in zero DC field due to significant quantum tunnelling of the magnetization (QTM). Nevertheless, QTM could be cancelled by applying an external DC field (Fig. S13–S15†). Field dependence of the magnetic susceptibility for **2–4Ln** were measured, and the relaxation times (τ) were extracted with an extended Debye model[57–59] (eqn (S1) and Tables S3–S5†) fitting simultaneously the two in-phase (χ'_M) and out-of-phase (χ''_M) components of magnetic susceptibility. The best fit of the field dependence of the relaxation time at 2 K was obtained using eqn (1).

$$\tau^{-1} = \frac{B_1}{1 + B_2 H^2} + 2B_3 H^m + B_4 \quad (1)$$

From left to right, the terms are the expressions of QTM, direct and thermally activated (Orbach + Raman) contributions. The best-fitted parameters for m fixed to 4 are: B_1 = 3.33(2) × 10^6 s^{-1}, B_2 = 8.85(6) × 10^{-3} Oe^{-2}, B_3 = 8.20(5) × 10^{-13} s^{-1} K^{-1} Oe^{-4} and B_4 = 29.25(6) s^{-1} for **3-Dy**, B_1 = 1.32(13) × 10^3 s^{-1}, B_2 = 7.71(15) × 10_{-6} Oe^{-2}, B_3 = 7.67(13) × 10^{-13} s^{-1} K^{-1} Oe^{-4} and B_4 = 7.95(13) × 10^2 s^{-1} for **2-Yb** and B_1 = 9.54(42) × 10^3 s^{-1}, B_2 = 1.83(1) × 10^{-5} Oe^{-2}, B_3 = 8.21(5) × 10^{-12} s^{-1} K^{-1} Oe^{-4} and B_4 = 60.03(51) × 10^2 s^{-1} for **4-Yb**. It is worth noting that the fits are used in a qualitative manner to evaluate the nature of the magnetic relaxation involved at 2 K under an applied magnetic field. Thus, the fitting procedure highlights that QTM, thermally activated mechanisms (Orbach + Raman) and direct relaxation processes are dominating in weak, moderate and high fields, respectively. The selected field, defined as a compromise between the relaxation time and the amplitude of the out-of-phase component, is 1000 Oe for **2-Yb**, **3-Dy** and **4-Yb**.

Under such an applied field, **2–4Ln** show frequency dependence of the out-of-phase signal of the magnetization (Fig. S16–S18†), which can be analysed in the framework of the extended Debye model.[57–59] The temperature dependence of

the relaxation time is plotted and depicted in Fig. 5d (Tables S6–S8†), and the normalized Argand (Fig. S19–S21†) concluded that more than 90% of the sample was slowly relaxing under the selected applied DC field. The thermal variation of the relaxation time could be fitted using eqn (2) for the three complexes considering a Raman process. For **3**, an additional Orbach process was identified for $T > 4$ K.

$$\tau^{-1} = \underbrace{CT^{n}}_{\text{Raman}} + \underbrace{\tau_0^{-1} \exp\left(-\frac{\Delta}{kT}\right)}_{\text{Orbach}} \quad (2)$$

The best fit was obtained with C = 36.7(8) K^{-n} s^{-1} and n = 4.53(2) for **2-Yb**, C = 8.2(3) K^{-n} s^{-1} with n = 2.96(2) and τ_0 = 2.12(11) × 10^{-6} s and Δ = 27.7(4) K (19 cm^{-1}) for **3-Dy** and C = 496.3(26) K^{-n} s^{-1} with n = 1.83(6) for **4-Yb**, where C and n are the constant and exponent factor of the Raman process, τ_0 and Δ are the relaxation time and the energy barrier of the Orbach relaxation process. The energy barrier found from the AC data (19 cm^{-1}) and *ab initio* calculation (31.8 cm^{-1}) are of the same order of magnitude. The expected n value for Kramers ions should be 9,[60] but it is well known that for molecular systems, the presence of both acoustic and optical phonons can lead to lower values comprised between 2 and 7[61–63] or even lower than 2 for some organometallic complexes and when phonon bottleneck process is involved.[64]

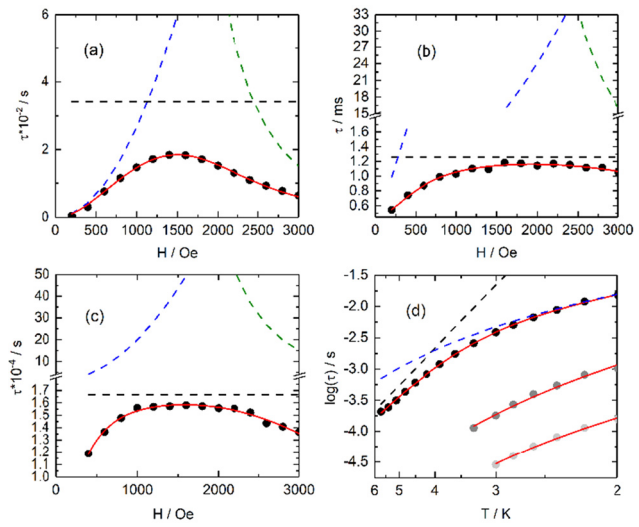

Fig. 5 Field dependence of the magnetic relaxation time (full black circles) at 2 K in the field range of 0–3000 Oe for **3-Dy** (a), **2-Yb** (b) and **4-Yb** (c) with the corresponding best fit depicted in the full red line. The separated thermally activated Orbach + Raman, QTM and direct processes are drawn in dashed black, blue and green lines, respectively. (d) Thermal dependence of the magnetic relaxation time for **2-Yb** under 1000 Oe applied magnetic field in the 2–3.4 K temperature range (full grey circles), for **3-Dy** under 1000 Oe applied magnetic field in the 2–5.7 K temperature range (full black circles) and for **4-Yb** under 1000 Oe applied magnetic field in the 2–3 K temperature range (full light grey circles). Full red lines are the best-fitted curves (see text) while the dashed lines are the Orbach (black) and Raman (blue) contributions.

As expected from the DC magnetic measurements, the two Yb(III) derivatives (**2-Yb** and **4-Yb**) behave similarly with field-induced SMM behaviour while the Dy(III) compounds show different magnetic behaviour with no slow magnetic relaxation for **1-Dy** and **5-Dy** but a field-induced SMM behaviour for **3-Dy**. This difference in SMM behaviour within the Dy series is well illustrated computationally by the magnetic transition moments calculated for **1-Dy** and **3-Dy** (Fig. S22†) and computed energy levels (Tables S9–S12†). Moreover, the main magnetic anisotropy axis appears perpendicular to the P═O–Dy–O═P direction and along the two $hfac^-$ anions, which are localized in the same plane. Such direction corresponds to the most charged orientation of the oblate Dy(III) ion coordination sphere (Fig. S23†) while the less charged orientation is preferred for the main component of the magnetic anisotropy axis in the case of prolate Yb(III) derivatives (**2-Yb** and **4-Yb**) (Fig. S24†).

Photophysical properties

The emission properties of the four mononuclear complexes **1–4Ln** were recorded at room temperature and at low temperature (77 K) in the solid state under 340 nm light irradiation. **1-Dy** displayed the classical visible emission of the Dy(III) ion attributed to the $^4F_{9/2} \rightarrow {}^6H_{n/2}$ transitions (Fig. 6a and Fig. S25†) while the two **2-Yb** and **4-Yb** complexes displayed the classical NIR Yb(III) centred emission attributed to the $^2F_{5/2} \rightarrow {}^2F_{7/2}$ transitions (Fig. 6b and Fig. S26†). On the contrary, **3-Dy** showed no metal-centred emission, probably because Dy(III) luminescence (475 nm, 21 053 cm^{-1}) is quenched by the too-low-energy triplet state of the tta^- anion in the $Ln(tta)_3$ moiety (527 nm, 18 975 cm^{-1}).[65] The emission spectra recorded at room temperature are not resolved enough to define the crystal field splitting of the ground state. Thus, emission measurements were carried out at liquid nitrogen temperature. At 77 K, the emission spectrum of **1-Dy** displayed eight contributions centred at 472.7 nm (21 155 cm^{-1}), 474.3 nm (21 084 cm^{-1}), 476.4 nm (20 991 cm^{-1}), 478.3 nm (20 907 cm^{-1}), 479 nm (20 877 cm^{-1}), 481.1 nm (20 786 cm^{-1}), 482.2 nm (20 738 cm^{-1}) and 489 nm (20 450 cm^{-1}). The confrontation with the excitation spectra (Fig. 6a) allowed us to attribute the two highest-energy lines to hot bands and the emission contribution at 20 991 cm^{-1} to the zero-phonon line. Thus, six of the eight expected contributions for the $^4F_{9/2} \rightarrow {}^6H_{15/2}$ transition could be identified while the two missing contributions cannot be unambiguously identified. The computational investigation suggested that the energy difference between the two lowest energy Kramers doublets (KDs) is very weak (7 cm^{-1}). Such a small energy gap was not observable on the luminescence spectrum of **1-Dy** but it was in agreement with the lack of slow magnetic relaxation. As already observed for similar Dy(III) coordination compounds,[66,67] the energy splitting for the $^6H_{15/2}$ ground state tends to be underestimated by calculation at the CASSCF level (Fig. 6a).

Irradiation at 340 nm of the solid-state samples of **2-Yb** and **4-Yb** at 77 K led to the observation of resolved Yb(III) centred emission spectra (Fig. 6b and Fig. S26†). Each spectrum dis-

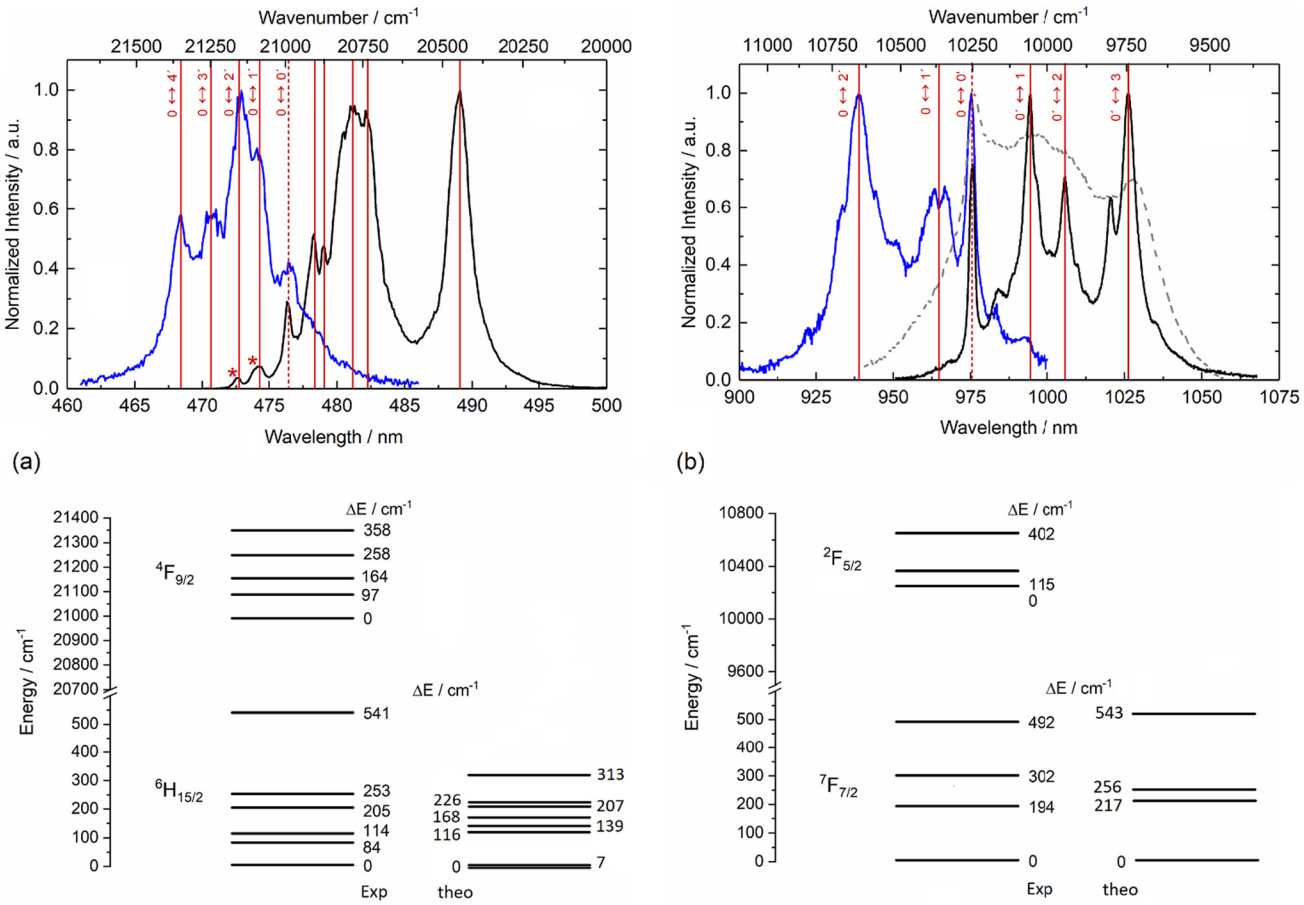

Fig. 6 Room (dashed grey line, only for Yb(III) derivatives) and low (full black line) temperature (77 K) solid-state emission spectra for **1-Dy** (a) and **2-Yb** (b) under irradiation at λ_{exc} = 340 nm and their corresponding excitation spectra (full blue line) obtained by detection at 490 nm for **1-Dy** and 1025 nm for **2-Yb**. The vertical red sticks represent the experimental energy splitting of the ground and first excited levels, with the dashed vertical sticks indicating the zero-phonon line. The corresponding energy diagrams of the ground and first excited state splitting for the two compounds are depicted at the bottom part of the corresponding spectra.

played the four main signals expected for the $^2F_{5/2} \rightarrow {}^2F_{7/2}$ transition. The energy differences between each experimentally observed m_J doublet correspond to the crystal field splitting of the $^2F_{7/2}$ ground state and are represented in the respective energy diagrams (right part of Fig. 6b and Fig. S26†). The measurements of the excitation spectra for both compounds led to the determination of the energy splitting for the $^2F_{5/2}$ excited state as well as the identification of the zero-phonon line. The energy splitting of both ground and excited states are similar for **2-Yb** and **4-Yb**, which is in agreement with their structural analysis. The total energy splitting for the ground state is 492 cm^{-1} for **2-Yb** and 529 cm^{-1} for **4-Yb**. Such total splitting values indicate low symmetrical coordination environments of the metal ion,[68,69] as already observed in previously reported compounds.[46] This splitting is well recovered at the CASPT2 level for **2-Yb**, especially the energy gap between the lowest KDs (ΔE_{exp} = 194 cm^{-1} and ΔE_{calc} = 217 cm^{-1}) (Fig. 6b) while it remains slightly too low in the case of **4-Yb** (ΔE_{exp} = 283 cm^{-1} and ΔE_{calc} = 121 cm^{-1}) (Fig. S26†). The poor agreement with the computed energy splitting for **4-Yb** (Fig. S26†) could be due to the uncertainties of the experimental emission contributions linked to the lower resolution of the **4-Yb** emission spectra compared to that of **2-Yb**. Additional emission lines can be identified for the two Yb(III) analogues, which can be attributed to hot bands and vibrational contributions.[47,48] The emission decay curves can be fitted by mono-exponential functions (Fig. S27†), confirming the presence of a single spectroscopic Yb(III) site and thus supporting the existence of single monomeric species in solution. The order of magnitude of the observed lifetimes (τ_{obs}) is τ_{obs} = 21.0 μs for **2-Yb** and 13.9 μs for **4-Yb**.

Conclusions

The reaction between the [2.2]paracyclophane-based Bisoxophosphine ligand and $[Ln(hfac)_3(H_2O)_2]$ or $[Ln(tta)_3(H_2O)_2]$ (Ln(III) = Dy and Yb) led to the formation of rare examples of lanthanide coordination complexes involving paracyclophane ligand. A dinuclear complex could be obtained

in the presence of NaBArF salt. The mononuclear complexes of formula [Yb(hfac)$_3$(**L**)] (**2-Yb**), [Dy(tta)$_3$(L)] (**3-Dy**) and [Yb(tta)$_3$(**L**)] (**4-Yb**) displayed field-induced SMM behaviour with magnetic relaxation occurring through the Raman process for **2-Yb** and **4-Yb**, and a combination of Orbach and Raman processes for **3-Dy**. The [2.2]paracyclophane decorated with two oxophosphine groups played the role of an organic chromophore for the efficient sensitization of both visible Dy(III) (for **1-Dy**) and near-infrared Yb(III) (for **2-Yb** and **4-Yb**) emissions. In cases of Yb(III) derivatives, magneto-structural correlation and comparison of both excitation and luminescence spectra led to the determination of the crystal field splitting of the $^2F_{7/2}$ ground state and $^2F_{5/2}$ first excited state. **2-Yb** and **4-Yb** can be described as unprecedented field-induced luminescent lanthanide SMMs involving paracyclophane ligands. The elaboration of the enantiopure complexes for chiroptical investigations is in progress in our laboratory.

Experimental section

Materials

The metal building blocks Ln(hfac)$_3$(H$_2$O)$_2$ (hfac$^-$ = 1,1,1,5,5,5-hexafluoroacetylacetonate anion)[70] and Ln(tta)$_3$(H$_2$O)$_2$ (tta$^-$ = 2-thenoyltrifluoroacetylacetonate anion)[71] (Ln = Dy(III) and Yb(III)) were synthesized following previously reported methods. Commercially available 4,16-dibromo[2.2]paracyclophane was purchased from Fisher Scientific and used as received. All other reagents were purchased from Merck Co., Inc. and used without further purification.

Synthesis

[2.2]paracyclophane decorated Bisoxophosphine ligand (L).[72]

*Synthesis of 4,12-dibromo[2.2]paracyclophane (**P2**).* In a 30 mL glass microwave vessel were added commercially available 4,16-dibromo[2.2]paracyclophane (**P1**, 1 equiv., 5 g, 13.6 mmol) and triglyme (20 mL). The reaction mixture was then heated to 220 °C in a microwave reactor. After 2 h, the reaction was cooled to room temperature, diluted with triglyme and the solid was filtered. The filtrate, which contains the reaction product, was diluted with water and extracted with diethyl ether (3×). The combined organic phases were washed with water and brine, dried over MgSO$_4$, and the solvents were evaporated under reduced pressure. The solid (starting material) was recovered and engaged once again in the isomerization reaction under microwave irradiation. This step was repeated until no more solids were recovered after the process. The combined crude products were purified *via* silica gel column chromatography using cyclohexane/ethyl acetate 9 : 1 as the eluent to obtain the desired product (4.2 g, 11.4 mmol, 84% yield) as a white solid. **^{1}H NMR** (500 MHz, CDCl$_3$): δ 7.19 (d, J = 1.6 Hz, 2H), 6.52 (dt, J = 7.8, 4.6 Hz, 4H), 3.45 (ddd, J = 13.3, 9.8, 2.0 Hz, 2H), 3.14–2.97 (m, 4H), 2.81 (ddd, J = 13.4, 10.3, 6.8 Hz, 2H) ppm. **^{13}C NMR** (125 MHz, CDCl$_3$): δ 141.3, 138.7, 135.0, 132.7, 131.6, 126.6, 35.8, 32.4 ppm. Spectroscopic data are consistent with the literature data for this compound.[73]

*Synthesis of 1,4(1,4)-dibenzenacyclohexaphane-1^2,4^3-diylbis (diphenylphosphine oxide) (**L**).* *tert*-Butyllithium (4 equiv., 13.7 mL, 21.85 mmol) was added dropwise over an hour to a solution of 4,12-dibromo[2.2]paracyclophane (**P2**, 1 equiv., 2 g, 5.46 mmol) in dry THF (60 mL) at −78 °C. After 15 minutes, the reaction mixture was allowed to warm up to room temperature, and diphenylphosphinic chloride (2.2 equiv., 2.29 mL, 12.02 mmol) was added. The reaction was stirred for 2 hours at rt, then poured into 2 N HCl (150 mL). The resulting aqueous mixture was extracted with CH_2Cl_2 (3×). The organic layers were combined, dried over MgSO$_4$, and the solvent was evaporated. The resulting solid was heated in an ethyl acetate/pentane mixture (2 : 3), then cooled and filtered to afford the desired ligand **L** (1.3 g, 2.46 mmol, 45% yield) as a white solid. **^{1}H NMR** (500 MHz, CDCl$_3$) δ 7.75–7.60 (m, 4H), 7.60–7.42 (m, 10H), 7.38 (td, J = 7.4, 1.2 Hz, 2H), 7.34–7.21 (m, 4H), 7.14 (dd, J = 14.6, 1.5 Hz, 2H), 6.76 (d, J = 7.6 Hz, 2H), 6.64 (dd, J = 7.6, 4.1 Hz, 2H), 3.35 (ddd, J = 12.6, 10.4, 6.7 Hz, 2H), 3.27–3.18 (m, 2H), 3.07–2.96 (m, 2H), 2.73 (ddd, J = 13.2, 10.4, 6.7 Hz, 2H). **^{13}C NMR** (125 MHz, CDCl$_3$): δ 144.7 (br), 139.6 (d, J = 12.8 Hz), 138.1 (d, J = 11.6 Hz), 135.3 (d, J = 11.2 Hz), 132.14 (d, J = 9.5 Hz), 131.9 (br), 131.7 (d, J = 1.6 Hz), 131.5 (br), 128.2 (d, J = 12.0 Hz), 35.7, 34.4. ^{31}P NMR (202 MHz, CDCl$_3$) δ 24.7 ppm. Spectroscopic data are consistent with the literature data for this compound.[73]

[Dy(hfac)$_3$(L)] (1-Dy). 1 equiv. (16.4 mg, 0.02 mmol) of Dy(hfac)$_3$(H$_2$O)$_2$ was dissolved in 5 mL of CH_2Cl_2 and 1 equiv. (12.2 mg, 0.02 mmol) of **L** was dissolved in 6 mL of CH_2Cl_2. The two resulting CH_2Cl_2 solutions were mixed and stirred for 30 minutes at room temperature. After this delay, 50 mL of n-hexane was layered. Slow diffusion, followed by slow evaporation, led to colourless single crystals that were suitable for X-ray studies. 16.7 mg, 60% yield. Anal. calcd (%) for $C_{55}H_{37}DyF_{18}O_8P_2$: C 47.40, H 2.66; found: C 47.32, H 2.71. I. R. (KBr, range 3200–500 cm^{-1}) 3061, 2946, 2865, 1657, 1554, 1528, 1506, 1256, 1204, 1144, 800, 684, 662 and 585 cm^{-1}.

[Yb(hfac)$_3$(L)] (2-Yb). A similar protocol as for **1-Dy** was employed using 16.7 mg of Yb(hfac)$_3$(H$_2$O)$_2$ instead of Dy(hfac)$_3$(H$_2$O)$_2$. 14.6 mg, 52% yield. Anal. Calcd (%) for $C_{55}H_{37}YbF_{18}O_8P_2$: C 47.08, H 2.64; found: C 47.12, H 2.66. I. R. (KBr, range 3200–500 cm^{-1}) 3060, 2946, 2865, 1655, 1554, 1528, 1503, 1258, 1204, 1144, 798, 685, 660 and 585 cm^{-1}.

[Dy(tta)$_3$(L)] (3-Dy). A similar protocol as for **1-Dy** was employed using 17.3 mg of Dy(tta)$_3$(H$_2$O)$_2$ instead of Dy(hfac)$_3$(H$_2$O)$_2$. 14.1 mg, 49% yield. Anal. Calcd (%) for $C_{64}H_{46}DyF_9O_8P_2S_3$: C 53.53, H 3.21; found: C 53.44, H 3.19. I. R. (KBr, range 3200–500 cm^{-1}) 3058, 2950, 2865, 1655, 1554, 1529, 1500, 1260, 1207, 1144, 799, 685, 660 and 584 cm^{-1}.

[Yb(tta)$_3$(L)] (4-Yb). A similar protocol as for **3-Dy** was employed using 18.0 mg of Yb(tta)$_3$(H$_2$O)$_2$ instead of Dy(tta)$_3$(H$_2$O)$_2$. 14.1 mg, 49% yield. Single crystals suitable for X-ray studies were obtained after recrystallization in toluene and diffusion of *n*-pentane. Anal. Calcd (%) for $C_{64}H_{46}YbF_9O_8P_2S_3$: C 53.14, H 3.18; found: C 53.11, H 3.22. I. R. (KBr, range 3200–500 cm^{-1}) 3061, 2954, 2865, 1650,

1552, 1529, 1499, 1261, 1207, 1144, 803, 685, 659 and 584 cm^{-1}.

[Na(Dy$_2$(hfac)$_6$(L)$_2$)](BArF) (5-Dy). 32.9 mg (0.04 mmol) of Dy(hfac)$_3$(H$_2$O)$_2$ and 35.4 mg (0.04 mmol) of NaBArF were dissolved in 5 mL of CH_2Cl_2, and 12.2 mg (0.02 mmol) of **L** was dissolved in 5 mL of CH_2Cl_2. The two resulting CH_2Cl_2 solutions were mixed and stirred for 30 minutes at room temperature. After this delay, 20 mL of *n*-hexane was layered. Slow diffusion, followed by slow evaporation, led to colourless single crystals that were suitable for X-ray studies. 12.5 mg, 17% yield. Anal. calcd (%) for $C_{142}H_{73}BDy_2F_{60}NaO_{16}P_4$: C 46.43, H 1.99; found: C 46.39, H 2.01. I. R. (KBr, range 3200–500 cm^{-1}) 3115, 3061, 2946, 2865, 1657, 1554, 1528, 1506, 1465, 1415, 1355, 1256, 1204, 1144, 801, 682, 660 and 583 cm^{-1}.

Material characterization

^{1}H NMR and ^{13}C NMR spectra were recorded on Bruker Avance 500 spectrometers operating at 500 (H value) and 125 MHz (C value) in $CDCl_3$. Spectra were referenced to the residual deuterated solvent (for $CHCl_3$: 7.26 ppm, ^{1}H; 77.16 ppm, ^{13}C). Chemical shifts are reported in ppm, and multiplicities are indicated by s (singlet), d (doublet), t (triplet), q (quartet) and m (multiplet or overlap of nonequivalent resonances), dd (doublet of doublet), td (triplet of doublet), and br (broad signal). Coupling constants, *J*, are reported in hertz (Hz). All NMR spectra were obtained at 300 K. Analytical thin layer chromatography (TLC) was performed on silica gel plates (Merck 60F254) visualized with a UV lamp (254 nm). Flash chromatography was performed on silica gel (60–230 mesh) unless otherwise specified. Organic extracts were dried over anhydrous $MgSO_4$. Microwave-mediated reactions were carried out using an Antoon Paar Monowave EXTRA. All solid-state characterization studies (elementary analysis, IR, PXRD, magnetic susceptibility and photophysical measurements) were performed on dried samples and are considered without crystallization solvents. The elemental analyses of the compounds were performed at the Centre Régional de Mesures Physiques de l'Ouest, Rennes.

X-ray structure analysis

Single crystals were mounted on a D8 VENTURE Bruker-AXS diffractometer for data collection for compounds **1–5** (MoKα radiation source, λ = 0.71073 Å) from the Centre de Diffractométrie X (CDIFX), Université de Rennes, France. Structures were solved with direct methods using the SHELXT Program[74] and refined with a full matrix least-squares method on F2 using the SHELXL-14/7 program.[75] Crystallographic data are summarized in Table S1.† Crystallographic data for the structure reported in this study have been deposited with the Cambridge Crystallographic Data Centre (insert CCDC 2297628–2297632† for **4-Yb**, **2-Yb**, **5-Dy**, **1-Dy** and **3-Dy**, respectively). X-ray diffraction (XRD) patterns were recorded at room temperature in the 2θ range 5–30° with a step size of 0.026° and a scan time per step of 600 s using a PANalytical X'Pert Pro diffractometer (Cu-L2, L3 radiation, λ = 1.5418 Å, 40 kV, 40 mA, PIXcel 1D detector). Data collector and HighScore Plus software were used, respectively, for recording and analysing the patterns.

Spectroscopic analysis

Luminescence spectra were measured using a Horiba-Jobin Yvon Fluorolog-3 spectrofluorimeter equipped with a three-slit double grating monochromator. The solid samples (crystalline powders) were placed in quartz tubes (4 mm diameter) and inserted in a quartz dewar that was filled with liquid nitrogen for low-temperature measurements. The excitation was provided by unpolarized light from a 450 W xenon CW lamp and detected at an angle of 90°. An 830 nm long-pass filter was placed between the sample and the detectors to avoid the presence of stray light due to excitation. Spectra were corrected for the emission spectral response (detector and grating). Near-infrared emission was recorded using a liquid nitrogen-cooled Symphony II CCD detector, and the corresponding excitation spectra were recorded using a liquid nitrogen-cooled solid indium/gallium/arsenic detector (850–1600 nm). Both emission and excitation in the UV/Vis region were recorded using a Hamamatsu R928 photomultiplier tube. For luminescence lifetimes, the sample was excited using a pulsed Nd:YAG laser (SpectraPhysics) operating at 10 Hz. Light emitted at right angles to the excitation beam was focused onto the slits of a monochromator (PTI120), which was used to select the appropriate wavelength. The growth and decay of the luminescence at selected wavelengths were detected using a Ge photodiode (Edinburgh Instruments, EI-P) and recorded using a digital oscilloscope (Tektronix TDS320) before being transferred for analysis. Luminescence lifetimes were obtained by iterative reconvolution of the detector response (obtained by using a scatterer) with exponential components for the growth and decay of the metal-centred luminescence.

Magnetic analysis

The DC magnetic susceptibility measurements were performed on a solid polycrystalline sample with a Quantum Design MPMS-XL SQUID magnetometer between 2 and 300 K in an applied magnetic field of 0.02 T for temperatures of 2–20 K, 0.2 T for temperatures of 20–80 K and 1 T for temperatures of 80–300 K. AC magnetic susceptibility measurements were performed using a Quantum Design MPMS-XL SQUID for frequencies between 1 and 1000 Hz and a Quantum Design PPMS magnetometers for frequencies between 50 and 10 000 Hz. These measurements were all corrected for diamagnetic contribution, as calculated with Pascal's constants.

Computational details

Wavefunction-based calculations were carried out on molecular structures of **1-Dy**, **2-Yb**, **3-Dy** and **4-Yb** complexes by using the SA-CASSCF/(MS-CASPT2)/RASSI-SO approach, as implemented in the OpenMolcas quantum chemistry package (versions 22.10).[76] In this approach, the relativistic effects are treated in two steps on the basis of the Douglas–Kroll Hamiltonian. First, the scalar terms were included in the

basis-set generation and were used to determine the spin-free wavefunctions and energies in the complete active space self-consistent field (CASSCF) method.[77] For **1-Dy** and **3-Dy**, the active space consisted of the nine 4f electrons of the Dy^{III} ion spanning the seven 4f orbitals, *i.e.*, CAS(9,7)SCF while for **2-Yb** and **4-Yb**, the active space consisted of thirteen 4f electrons of the Yb^{III} ion spanning the seven 4f orbitals, *i.e.* CAS(13,7)SCF. In order to obtain a better description of the electronic structure of the Ytterbium systems (**2-Yb** and **4-Yb**), calculations were computed using perturbation theory at the second order,[78] *i.e.*, MS-CAS(13,7)PT2, based on the previous CAS (13,7)SCF results. Next, spin–orbit coupling was added within the restricted-active-space-state-interaction (RASSI-SO) method, which uses spin-free wavefunctions as basis states.[79,80] Spin–orbit (SO) integrals are calculated using the AMFI (atomic mean-field integrals) approximation.[81] The resulting wavefunctions and energies are used to compute the magnetic properties and g-tensors of the lowest states from the energy spectrum using the pseudo-spin $S = 1/2$ formalism in the SINGLE-ANISO routine.[82,83] Cholesky decomposition of the bielectronic integrals was employed to save disk space and speed up the calculations.[84] For **1-Dy** and **3-Dy**, state-averaged CASSCF calculations were performed for all of the sextets (21 roots), all of the quadruplets (224 roots), and 300 out of the 490 doublets of the Dy^{III} ion. 21 sextets, 128 quadruplets, and 107 doublets were mixed through spin–orbit coupling in RASSI-SO. For **2-Yb** and **4-Yb**, state-averaged CASSCF calculations were performed for the 7 doublets. All atoms were described by ANO-RCC basis sets.[85,86] The following contractions were used: [8s7p4d3f2g1h] for Dy and Yb, [4s3p2d] for the O atoms, [4s3p] for the P and S atoms, [3s2p] for the C and F atoms and [2s] for the H atoms. The atomic positions were extracted from the X-ray crystal structures. Only the positions of the H atoms were optimized with the AMS program suite (revision 2022.103).[87,88] These calculations utilized the scalar all-electron zeroth-order regular approximation (ZORA)S15 along with the revPBE (Perdew–Burke–Ernzerhof) functional.[89,90] For all atoms, the atomic basis set corresponded to the triple-ζ polarized (TZP) Slater-type orbital (STO) all-electron basis set.[91]

Author contributions

J. B. and E. B. performed the organic syntheses, H. F. performed the coordination chemistry and crystallisations; V. D. realised the single crystal X-ray diffraction experiments and refined the X-ray structures; T. G. and O. C. performed and analysed the magnetic measurements. B. L. G. performed the computational investigation. A. S. and O.M. investigated the absorption and emission properties. L. M. and E. B. discussed the idea and the results and commented on the manuscript. F. P. conceived and designed the experiments and drove the writing of the article. All authors have read and agreed on the published version of the manuscript.

Conflicts of interest

The authors declare no conflicts of interest.

Acknowledgements

This work was supported by CNRS, Université de Rennes, the European Research Council through the ERC-CoG 725184 MULTIPROSMM (project no. 725184) and the Agence Nationale de la Recherche (SMMCPL ANR-19-CE29-0012-02; PhotoChiraPhane ANR-19-CE07-0001). B. L. G. thanks the French GENCI/IDRIS-CINES centres for high-performance computing resources. Yannick Guyot is acknowledged for the luminescence lifetime measurements.

References

1 C. J. Brown and A. C. Farthing, *Nature*, 1949, **164**, 915–916.
2 H. Hope, J. Bernstein and K. N. Trueblood, *Acta Crystallogr., Sect. B: Struct. Crystallogr. Cryst. Chem.*, 1972, **28**, 1733–1743.
3 G. P. Bartholomew, I. Ledoux, S. Mukamel, G. C. Bazan and J. Zyss, *J. Am. Chem. Soc.*, 2002, **124**, 13480–13485.
4 D. J. Cram and N. L. Allinger, *J. Am. Chem. Soc.*, 1955, **77**, 6289.
5 S. Felder, M.-L. Delcourt, R. Rodríguez, L. Favereau, J. Crassous, L. Micouin and E. Benedetti, *J. Mater. Chem. C*, 2023, **11**, 2053–2062.
6 Z. Hassan, E. Spuling, D. M. Knoll, J. Lahann and S. Bräse, *Chem. Soc. Rev.*, 2018, **47**, 6947–6963.
7 S. E. Gibson and J. D. Knight, *Org. Biomol. Chem.*, 2003, **1**, 1256–1269.
8 N. Ishikawa, M. Sugita, T. Ishikawa, S. Koshihara and Y. Kaizu, *J. Am. Chem. Soc.*, 2003, **125**, 8694–8695.
9 R. Sessoli, D. Gatteschi, A. Caneschi and M. A. Novak, *Nature*, 1993, **365**, 141–143.
10 M. Mannini, F. Pineider, P. Sainctavit, C. Danieli, E. Otero, C. Sciancalepore, A. M. Talarico, M.-A. Arrio, A. Cornia, D. Gatteschi and R. Sessoli, *Nat. Mater.*, 2009, **8**, 194–197.
11 S. Thiele, F. Balestro, R. Ballou, S. Klyatskaya, M. Ruben and W. Wernsdorfer, *Science*, 2014, **344**, 1135–1138.
12 K. S. Pedersen, A.-M. Ariciu, S. McAdams, H. Weihe, J. Bendix, F. Tuna and S. Piligkos, *J. Am. Chem. Soc.*, 2016, **138**, 5801–5804.
13 J. D. Rinehart, M. Fang, W. K. Evans and J. R. Long, *Nat. Chem.*, 2011, **3**, 538–542.
14 S. Demir, J. M. Zadrozny, M. Nippe and J. R. Long, *J. Am. Chem. Soc.*, 2012, **134**, 18546–18549.
15 R. A. Layfield, M.-L. Tong, B. M. Day, Y.-C. Chen, F.-S. Guo and A. Mansikkamaki, *Science*, 2018, **362**, 1400–1403.
16 K. R. McClain, C. A. Gould, K. Chakarawet, S. J. Teat, T. J. Groshens, J. R. Long and B. G. Harvey, *Chem. Sci.*, 2018, **9**, 8492–8503.

17 C. A. P. Goodwin, F. Ortu, D. Reta, N. F. Chilton and D. P. Mills, *Nature*, 2017, **548**, 439–442.
18 A. H. Vincent, Y. L. Whyatt, N. F. Chilton and J. R. Long, *J. Am. Chem. Soc.*, 2023, **145**, 1572–1579.
19 C. A. Gould, K. R. McClain, D. Reta, J. G. C. Kragskow, D. A. Marchiori, E. Lachman, E.-S. Choi, J.-G. Analytis, R. D. Britt, N. F. Chilton, B. G. Harvey and J. R. Long, *Science*, 2022, **375**, 198–202.
20 J.-C. G. Bünzli, *Acc. Chem. Res.*, 2006, **39**, 53–61.
21 S. V. Eliseeva and J.-C. G. Bünzli, *Chem. Soc. Rev.*, 2010, **39**, 189.
22 S. V. Eliseeva and J.-C. G. Bünzli, in *Lanthanide spectroscopy, Materials, and Bioapplications, Springer Series on Fluorescence*, ed. P. Hänninen and H. Härmä, Springer, Verlag, Berlin, 2010, vol. 7; *Luminescence of Lanthanide Ions in Coordination Compounds and Nanomaterials*, ed. A. De Bettencourt-Diaz, Wiley, New York, 2014.
23 C. P. Montgomery, B. S. Murray, E. J. New, R. Pal and D. Parker, *Acc. Chem. Res.*, 2009, **42**, 925–937.
24 E. G. Moore, A. P. S. Samuel and K. N. Raymond, *Acc. Chem. Res.*, 2009, **42**, 542–552.
25 A. D'Aleo, A. Bourdolle, S. Bulstein, T. Fauquier, A. Grichine, A. Duperray, P. L. Baldeck, C. Andraud, S. Brasselet and O. Maury, *Angew. Chem., Int. Ed.*, 2012, **51**, 6622–6625.
26 S. Banerjee, L. Huebner, M. D. Romanelli, G. A. Kumar, R. E. Riman, T. J. Emge and J. G. Brennan, *J. Am. Chem. Soc.*, 2005, **127**, 15900–15906.
27 G. A. Kumar, R. E. Riman, L. A. Diaz Torres, S. Banerjee, M. D. Romanelli, T. J. Emge and J. G. Brennan, *Chem. Mater.*, 2007, **19**, 2937–2946.
28 S. Banerjee, G. A. Kumar, R. E. Riman, T. J. Emge and J. G. Brennan, *J. Am. Chem. Soc.*, 2007, **129**, 5926–5931.
29 M. Romanelli, G. A. Kumar, T. J. Emge, R. E. Riman and J. G. Brennan, *Angew. Chem., Int. Ed.*, 2008, **47**, 6049–6051.
30 L. Song, X. Liu, Z. Zhen, C. Chen and D. Zhang, *J. Mater. Chem.*, 2007, **17**, 4586–4590.
31 M. D. McGehee, T. Bergstedt, C. Zhang, A. P. Saab, M. B. O'Regan, G. C. Bazan, V. I. Srdanov and A. J. Heeger, *Adv. Mater.*, 1999, **11**, 1349–1354.
32 A. de Bettencourt-Dias, *Dalton Trans.*, 2007, 2229–2241.
33 F. Pointillart, B. Le Guennic, O. Cador, O. Maury and L. Ouahab, *Acc. Chem. Res.*, 2015, **48**, 2834–2842.
34 J. H. Jia, Q.-W. Li, Y.-C. Chen, J.-L. Liu and M.-L. Tong, *Coord. Chem. Rev.*, 2019, **378**, 365–381.
35 R. Marin, G. Brunet and M. Murugesu, *Angew. Chem., Int. Ed.*, 2021, **60**, 1728–1746.
36 G. Brunet, R. Marin, M.-J. Monk, U. Resch-Genger, D. A. Gálico, F. A. Sigoli, E. A. Suturina, E. Hemmer and M. Murugesu, *Chem. Sci.*, 2019, **10**, 6799–6808.
37 J. Wang, J. J. Zakrzewski, M. Heczko, M. Zychowicz, K. Nakagawa, K. Nakabayashi, B. Sieklucka, S. Chorazy and S. Ohkoshi, *J. Am. Chem. Soc.*, 2020, **142**, 3970–3979.
38 D. Errulat, R. Marin, D. A. Gálico, K. L. M. Harriman, A. Pialat, B. Gabidullin, F. Iikawa, O. D. D. Couto Jr, J. O. Moilanen, E. Hemmer, F. A. Sigoli and M. Murugesu, *ACS Cent. Sci.*, 2019, **5**, 1187–1198.
39 P.-Y. Liao, Y. Liu, Z.-Y. Ruan, H.-L. Wang, C.-G. Shi, W. Deng, S.-G. Wu, J.-H. Jia and M.-L. Tong, *Inorg. Chem.*, 2023, **62**, 1075–1085.
40 Y. B. Tan, Y. Okayasu, S. Katao, Y. Nishikawa, F. Asanoma, M. Yamada, J. Yuasa and T. Kawai, *J. Am. Chem. Soc.*, 2020, **142**, 17653–17661.
41 J. L. Lunkley, D. Shirotani, K. Yamanari, S. Kaizaki and G. Muller, *J. Am. Chem. Soc.*, 2008, **130**, 13814–13815.
42 O. G. Willis, F. Zinna, G. Pescitelli, C. Micheletti and L. Di Bari, *Dalton Trans.*, 2022, **51**, 518–523.
43 N. F. M. Mukthar, N. D. Schley and G. Ung, *J. Am. Chem. Soc.*, 2022, **144**, 6148–6153.
44 B.-A. N. Willis, D. Schnable, N. D. Schley and G. Ung, *J. Am. Chem. Soc.*, 2022, **144**, 22421–22425.
45 C. A. Mattei, K. Dhbaibi, B. Lefeuvre, V. Dorcet, G. Argouarch, O. Cador, B. Le Guennic, O. Maury, C. Lalli, S. Guy, A. Bensalah-Ledoux, F. Riobé, B. Baguenard and F. Pointillart, *Chirality*, 2021, 1–14.
46 C. A. Mattei, V. Montigaud, B. Lefeuvre, V. Dorcet, G. Argouarch, O. Cador, B. Le Guennic, O. Maury, C. Lalli, Y. Guyot, S. Guy, C. Gindre, A. Bensalah-Ledoux, F. Riobé, B. Baguenard and F. Pointillart, *J. Mater. Chem.*, 2023, **11**, 7299–7310.
47 M. Atzori, K. Dhbaibi, H. Douib, M. Grasser, V. Dorcet, I. Breslavetz, K. Paillot, O. Cador, G. L. J. A. Rikken, B. Le Guennic, J. Crassous, F. Pointillart and C. Train, *J. Am. Chem. Soc.*, 2021, **143**, 2671–2675.
48 K. Dhbaibi, M. Grasser, H. Douib, V. Dorcet, O. Cador, N. Vanthuyne, F. Riobé, O. Maury, S. Guy, A. Bensalah-Ledoux, B. Baguenanrd, G. L. J. A. Rikken, C. Train, B. Le Guennic, M. Atzori, F. Pointillart and J. Crassous, *Angew. Chem., Int. Ed.*, 2023, e202215558.
49 R. Grykien, B. Luszczynska, I. Glowacki, L. Puntus, I. Pekareva, K. Lyssenko, F. Kajzar, I. Rau and C. A. Lazar, *Opt. Mater.*, 2016, **57**, 114–119.
50 S. Wu, L. Abad Galan, M. Roux, F. Riobé, B. Le Guennic, Y. Guyot, T. Le Bahers, L. Micouin, O. Maury and E. Benedetti, *Inorg. Chem.*, 2021, **60**, 16194–16203.
51 M. Llunell, D. Casanova, J. Cirera, P. Alemany and S. Alvarez, *SHAPE Program for the Stereochemical Analysis of Molecular Fragments by Means of Continuous Shape Measures and Associated Tools*, Departament de Quimica Fisica, Departament de Quimica Inorganica, and Institut de Quimica Teorica i Computacional – Universitat dè Barcelona, Barcelona, Spain.
52 H. Douib, K. Dhbaibi, B. Lefeuvre, V. Dorcet, T. Guizouarn and F. Pointillart, *Chirality*, 2022, 1–10.
53 C. Benelli and D. Gatteschi, *Introduction to Molecular Magnetism: From Transition Metals to Lanthanides*, Wiley-VCH Verlag GmbH & Co. KGaA, Weinheim, Germany, 2015.
54 O. Kahn, *Molecular Magnetism*, VCH, Weinhem, Germany, 1993.
55 J. Jung, T. T. da Cunha, B. Le Guennic, F. Pointillart, C. L. M. Pereira, J. Luzon, S. Golhen, O. Cador, O. Maury and L. Ouahab, *Eur. J. Inorg. Chem.*, 2014, 3888–3894.

56 F. Gendron, S. Di Pietro, L. Abad Galan, F. Riobé, V. Placide, L. Guy, F. Zinna, L. Di Bari, A. Bensalah-Ledoux, Y. Guyot, G. Pilet, F. Pointillart, B. Baguenard, S. Guy, O. Cador, O. Maury and B. Le Guennic, *Inorg. Chem. Front.*, 2021, **8**, 914–926.
57 K. S. Cole and R. H. Cole, *J. Chem. Phys.*, 1941, **9**, 341–351.
58 R. Orbach, *Proc. R. Soc. London, Ser. A*, 1961, **264**, 458–484.
59 R. Orbach, *Proc. Phys. Soc.*, 1961, **77**, 821–826.
60 C. Dekker, A. F. M. Arts, H. W. de Wijn, A. J. van Duyneveldt and J. A. Mydosh, *Phys. Rev. B: Condens. Matter Mater. Phys.*, 1989, **40**, 11243–11251.
61 J. Tang and P. Zhang, *Lanthanide Single Molecule Magnets*, Springer, Berlin, Germany, 2015.
62 P. Evans, D. Reta, G. F. S. Whitehead, N. F. Chilton and D. P. Mills, *J. Am. Chem. Soc.*, 2019, **141**, 19935–19940.
63 D. Reta and N. F. Chilton, *Phys. Chem. Chem. Phys.*, 2019, **21**, 23567–23575.
64 K. N. Shrivastava, *Phys. Status Solidi B*, 1983, **117**, 437–458.
65 H. Xu, L.-H. Wang, X.-H. Zhu, K. Yin, G.-Y. Zhong, X.-Y. Hou and W. Huang, *J. Phys. Chem. B*, 2006, **110**, 3023–3029.
66 C. A. Mattei, V. Montigaud, F. Gendron, S. Denis-Quantin, V. Dorcet, N. Giraud, F. Riobé, G. Argouarch, O. Maury, B. Le Guennic, O. Cador, C. Lalli and F. Pointillart, *Inorg. Chem. Front.*, 2021, **8**, 947–962.
67 C. A. Mattei, V. Montigaud, V. Dorcet, F. Riobé, G. Argouarch, O. Maury, B. Le Guennic, O. Cador, C. Lalli and F. Pointillart, *Inorg. Chem. Front.*, 2021, **8**, 963–976.
68 Y. Kishi, L. Cornet, F. Pointillart, F. Riobé, B. Lefeuvre, O. Cador, B. Le Guennic, O. Maury, H. Fujiwara and L. Ouahab, *Eur. J. Inorg. Chem.*, 2018, 458–468.
69 F. Guégan, J. Jung, B. Le Guennic, F. Riobé, O. Maury, B. Gillon, J.-F. Jacquot, Y. Guyot, C. Morel and D. Luneau, *Inorg. Chem. Front.*, 2019, **6**, 3152–3157.
70 M. F. Richardson, W. F. Wagner and D. E. Sands, *J. Inorg. Nucl. Chem.*, 1968, **30**, 1275–1289.
71 A. I. Vooshin, N. M. Shavaleev and V. P. Kazakov, *J. Lumin.*, 2000, **91**, 49–58.
72 S. Felder, S. Wu, J. Brom, L. Micouin and E. Benedetti, *Chirality*, 2021, **33**, 506–527.
73 P. J. Pye, K. Rossen, R. A. Reamer, N. N. Tsou, R. P. Volante and P. J. Reider, *J. Am. Chem. Soc.*, 1997, **119**, 6207–6208.
74 G. M. Sheldrick, *Acta Crystallogr., Sect. C: Struct. Chem.*, 2015, **71**, 3–8.
75 A. L. Spek, *J. Appl. Crystallogr.*, 2003, **36**, 7–13.
76 I. F. Galván, M. Vacher, A. Alavi, C. Angeli, F. Aquilante, J. Autschbach, J. J. Bao, S. I. Bokarev, N. A. Bogdanov, R. K. Carlson, L. F. Chibotaru, J. Creutzberg, N. Dattani, M. G. Delcey, S. S. Dong, A. Dreuw, L. Freitag, L. M. Frutos, L. Gagliardi, F. Gendron, A. Giussani, L. González, G. Grell, M. Guo, C. E. Hoyer, M. Johansson, S. Keller, S. Knecht, G. Kovačević, E. Källman, G. Li Manni, M. Lundberg, Y. Ma, S. Mai, J. P. Malhado, P. Å. Malmqvist, P. Marquetand, S. A. Mewes, J. Norell, M. Olivucci, M. Oppel, Q. M. Phung, K. Pierloot, F. Plasser, M. Reiher, A. M. Sand, I. Schapiro, P. Sharma, C. J. Stein, L. K. Sørensen, D. G. Truhlar, M. Ugandi, L. Ungur, A. Valentini, S. Vancoillie, V. Veryazov, O. Weser, T. A. Wesołowski, P.-O. Widmark, S. Wouters, A. Zech, J. P. Zobel and R. Lindh, *J. Chem. Theory Comput.*, 2019, **15**, 5925–5964.
77 B. O. Roos, P. R. Taylor and P. E. M. Siegbahn, *Chem. Phys.*, 1980, **48**, 157–173.
78 K. Andersson, P.-Å. Malmqvist, B. O. Roos, A. J. Sadlev and K. Wolinski, *J. Phys. Chem.*, 1990, **94**, 5483–5488.
79 P.-A. Malmqvist, B. O. Roos and B. Schimmelpfennig, *Chem. Phys. Lett.*, 2002, **357**, 230–240.
80 P.-A. Malmqvist and B. O. Roos, *Chem. Phys. Lett.*, 1989, **155**, 189–194.
81 B. A. Heß, C. M. Marian, U. Wahlgren and O. Gropen, *Chem. Phys. Lett.*, 1996, **251**, 365–371.
82 L. F. Chibotaru and L. Ungur, *J. Chem. Phys.*, 2012, **137**, 064112.
83 L. F. Chibotaru, L. Ungur and A. Soncini, *Angew. Chem., Int. Ed.*, 2008, **47**, 4126–4129.
84 F. Aquilante, P.-A. Malmqvist, T. B. Pedersen, A. Ghosh and B. O. Roos, *J. Chem. Theory Comput.*, 2008, **4**, 694–702.
85 B. O. Roos, R. Lindh, P.-A. Malmqvist, V. Veryazov and P.-O. Widmark, *J. Phys. Chem. A*, 2004, **108**, 2851–2858.
86 B. O. Roos, R. Lindh, P.-A. Malmqvist, V. Veryazov, P.-O. Widmark and A.-C. Borin, *J. Phys. Chem. A*, 2008, **112**, 11431–11435.
87 G. te Velde, F. M. Bickelhaupt, E. J. Baerends, C. Fonseca Guerra, S. J. A. van Gisbergen, J. G. Snijders and T. Ziegler, *J. Comput. Chem.*, 2001, **22**, 931–967.
88 AMS 2022.103, Amsterdam, The Netherlands, **https://www.scm.com**.
89 J. P. Perdew, K. Burke and M. Ernzerhof, *Phys. Rev. Lett.*, 1996, **77**, 3865–3868.
90 J. P. Perdew, K. Burke and M. Ernzerhof, *Phys. Rev. Lett.*, 1997, **78**, 1396.
91 E. van Lenthe and E. J. Baerends, *J. Comput. Chem.*, 2003, **24**, 1142–1156.